

Control system development for the snowflake divertor on NSTX-U

P. J. Vail¹, E. Kolemen¹, M. D. Boyer², A. S. Welander³

¹ Department of Mechanical and Aerospace Engineering, Princeton University, Princeton, New Jersey, USA

² Princeton Plasma Physics Laboratory, Princeton, New Jersey, USA

³ General Atomics, San Diego, California, USA

E-mail: pjv@princeton.edu

Abstract. This paper presents the development of a model-based multiple-input-multiple-output algorithm for real-time feedback control of snowflake divertor configurations on the National Spherical Torus eXperiment Upgrade (NSTX-U). A linearized time-varying model of the snowflake configuration response to applied voltages on the divertor control coils is derived and then used, in conjunction with multivariable control synthesis techniques, to design an optimal state feedback controller for the configuration. Control system performance is then validated using a closed-loop simulator that evolves linear models of the coil and vessel current dynamics simultaneously with the free-boundary plasma equilibrium. Simulations demonstrate that the algorithm enables controlled operations in a variety of snowflake configurations and provides capabilities for accurate tracking of time-dependent reference trajectories for the divertor configuration.

1. Introduction

The National Spherical Torus eXperiment Upgrade (NSTX-U) [1] is a mega-ampere grade spherical tokamak (ST) at the Princeton Plasma Physics Laboratory (PPPL) that has been constructed to enhance the physics and engineering understanding required for building future ST-based fusion devices, such as those intended for studying plasma-material interactions [2], testing nuclear reactor components [3], and demonstrating fusion power generation [4]. NSTX-U is designed to improve upon the performance of prior STs such as NSTX [5] and the Mega-Ampere Spherical Tokamak (MAST) [6] and will enable access to new plasma regimes for the study of critical issues such as the scaling of energy confinement with electron collisionality, the physics of fast particles, and the efficiency of methods for non-inductive current drive in high- β scenarios. Significant upgrades to the NSTX-U device were recently completed, including the installation of a larger-diameter centerstack and a second neutral beam injection system. The new centerstack, which contains the inner legs of the toroidal field (TF) coils, the Ohmic heating (OH) solenoid, and several plasma shaping coils, provides higher fluxes and fields for increasing plasma confinement and extending the duration of plasma discharges. The second neutral beam injector increases the auxiliary heating power (5 to 10 MW) and current drive and is aimed more tangentially, thereby enabling greater control of the spatial distribution of heating and current. The upgrades will increase the nominal TF from 0.5 to 1T, the maximum plasma current from 1 to 2 MA, and will enable plasma discharge durations of up to 5s.

1.1. Motivation for advanced divertor configurations on NSTX-U

Routine plasma operations in high-performance scenarios (2 MA, 1T, 10 MW) is a crucial prerequisite for achieving many of the goals of the NSTX-U research program. As a primary example, higher plasma current and toroidal field are required on NSTX-U to distinguish between conventional aspect ratio and ST confinement time scaling, and a corresponding increase in input heating power is required for achieving sufficient plasma- β at these higher currents and fields. Furthermore, a target discharge duration of 5s is motivated by a need to ensure sufficient current profile equilibration in high confinement, low density plasma regimes [7]. A consequence of these device requirements is that a variety of novel technologies and operational strategies will be needed for achieving safe and reliable high-performance discharges on NSTX-U. Since the early stages of the upgrade, it has been recognized that one of the most critical issues for NSTX-U will be the power loading of plasma-facing components (PFCs) in the divertor region. While heat flux management is a concern for many current and future devices, it is of particular importance for STs due to their compact size. In [1], it was shown that in the NSTX-U high-performance scenario with 2 MA, 10 MW, and 5s pulse length, the peak heat flux on divertor surfaces cannot exceed 10 MW/m² without compromising the structural integrity of the radiatively-cooled PFCs. Since the start of NSTX-U plasma operations, the requirements for heat flux mitigation have grown more stringent as the

design of the divertor PFCs is re-evaluated during the NSTX-U recovery project. This analysis incorporates more recent developments in the fusion community, including the identification of significant uncertainty in the scaling of the heat flux width λ_q for STs. Indeed, the projected values of λ_q for NSTX-U as computed by several recently-proposed empirical and semi-empirical models vary by up to a factor of two [8, 9, 10, 11], thereby leading to a corresponding uncertainty in the peak power deposited on the divertor.

A combination of heat flux mitigation strategies is currently planned for use on NSTX-U, including controlled sweeping of the divertor strike point to vary the location of peak power loading, operating in a double-null configuration to enable sharing of the power exhaust between the up-down symmetric divertor PFCs, and adding divertor fueling capabilities to increase the radiated power fraction. Another promising means of reducing the peak heat flux on divertor PFCs is the use of so-called advanced divertor configurations, such as the snowflake divertor [12], X-divertor [13], super-X divertor [14], and X-point target divertor [15], all of which are magnetic topologies that differ in some way from that of the standard axisymmetric X-point divertor. In particular, the snowflake divertor (SFD) is being considered as one component of an integrated power exhaust solution on NSTX-U. The exact SFD configuration has a second-order null on the primary separatrix and is characterized by a magnetic topology with a hexagonal structure resembling a snowflake. Due to the extreme sensitivity of the exact SFD configuration to small deviations from the electric current distribution that defines this equilibrium, one of two alternative configurations is generally observed: (1) the snowflake-plus configuration with a primary X-point on the separatrix and a secondary X-point in the private flux region, and (2) the snowflake-minus configuration in which the secondary X-point lies in the scrape-off layer (SOL). Figure 1 depicts three simulated snowflake equilibria on NSTX-U, including the required coil currents for each configuration, as well as a standard single-null equilibrium for comparison.

As summarized in [16], the SFD has several properties that are advantageous for reducing divertor PFC heat fluxes: Due to the reduced poloidal field magnitude in the null region, the SFD exhibits stronger flaring of magnetic field lines and increased poloidal flux expansion relative to the standard divertor. The result is a greatly increased plasma wetted-area and a corresponding decrease in the peak heat flux. The need for high flux expansion divertors to mitigate power exhaust is the primary motivation for the development of SFD scenarios on NSTX-U. Additional properties of the configuration include a significantly longer X-point connection length, leading to an increase in the temperature drop and radiative losses in the SOL, and the presence of additional strike points across which the power exhaust can be partitioned. In recent years, the SFD has been the subject of investigations on several devices [17, 18, 19, 20], all of which have provided experimental confirmation of many favorable properties of the snowflake magnetic configuration. In particular, the SFD was integrated into H-mode scenarios on NSTX (prior to the upgrade). It was determined using equilibrium reconstructions of 1 MA, 0.5T, 5 MW NBI-heated discharges that the flux expansion in the SOL was nearly four times higher than in the standard divertor, while the X-point connection

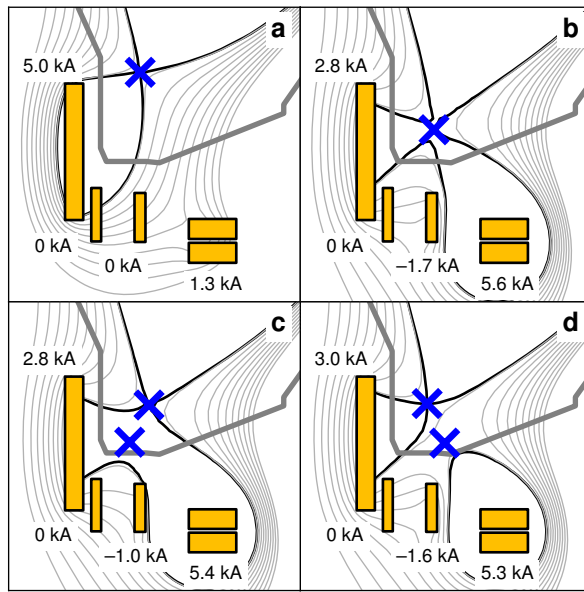


Figure 1. Several divertor configurations on NSTX-U as computed by a free-boundary equilibrium solver with $I_p = 1$ MA, $\beta_p = 1.0$, and $l_i = 0.6$. Shown are (a) the standard single-null divertor, (b) the exact snowflake configuration with a second-order null, (c) the snowflake-plus configuration with a secondary null in the private flux region, and (d) the snowflake-minus configuration with a secondary null in the scrape-off layer. Also shown are the divertor coils and coil currents for each configuration.

length was double that of the standard configuration. The existence of these favorable magnetic properties was accompanied by a significant reduction in the peak heat flux on the divertor (from roughly 5 to 1 MW/m²) as measured by infrared diagnostics. Furthermore, no degradation of core and pedestal performance, as quantified by metrics such as confinement time, β_N , and stored energy, was exhibited during plasma operations in the snowflake configuration. Future experiments will seek to assess the performance of the SFD at the higher current, field, and input heating power that are projected for NSTX-U.

1.2. Overview of magnetic control for the snowflake divertor

While the SFD may prove to be an enabling technology for NSTX-U (as well as for future devices such as ITER and DEMO [21]) due to its favorable magnetic field properties, the snowflake configuration presents new challenges for real-time plasma operations. In particular, it has been recognized since the advent of the SFD concept that feedback control is required to regulate the configuration during plasma discharges due to the inherent complexity of the SFD magnetic topology and the control limitations stemming from the coil configurations on most tokamaks. Due to the sensitivity of the second-order field null in the exact SFD, one must normally account for the locations of two closely-spaced X-points in the SFD-plus or SFD-minus configurations. Unlike in the standard divertor configuration, the proximate X-points of the SFD present two candidates for

the flux which defines the plasma boundary. While of little consequence for the global shape and positioning of the plasma due to the shallow field gradients in the vicinity of the X-points, the identity of the boundary-defining point in the snowflake configuration has a significant impact on divertor performance since a modification of the boundary flux can cause a large shift in the locations of active strike points. Furthermore, the relative positioning of the two X-points, quantified by parameters such as the inter-null distance and the orientation of the line segment connecting the nulls (roughly speaking, the radius and angle in a polar coordinate system), determines critical SFD properties such as flux expansion, connection length, and power exhaust partitioning among strike points. Aside from the intrinsic geometric complexities of the SFD, it is often the case that fewer shape control coils are available on a particular device than are required for simultaneous control of all parameters that define the configuration. In most cases, there is also significant cross-coupling between the divertor control coils. The unique challenges presented by the SFD for real-time control therefore motivate the development of a sophisticated multiple-input-multiple-output (MIMO) divertor control algorithm for the snowflake configuration.

Over the last several years, various solutions to the SFD control problem have been proposed and tested experimentally. TCV has used extensive offline modeling to determine coil currents that are consistent with desired snowflake equilibria [17]. The coil currents are then pre-programmed as targets for the control system to track during real-time operations. On NSTX, the first experiments in which the SFD configuration was achieved employed a combined feedforward-feedback hybrid approach in which the primary divertor coils were used to control the locations of the inner and outer strike points, while the currents in secondary coils were modified in a gradient-search fashion to determine values of the plasma squareness ζ and δR_{sep} that were consistent with a snowflake equilibrium [22, 23]. Based upon modeling of SFD configurations on NSTX using the free-boundary Grad-Shafranov equilibrium code ISOLVER [24], it was determined that the use of three divertor coils would enable refined control of the SFD. In further experiments on NSTX, therefore, a primary divertor coil was used in a feedback loop to control the location of the primary X-point, while two secondary coils executed pre-programmed current ramps to push the secondary X-point into the vacuum vessel [18]. These combined feedforward-feedback control approaches on NSTX were sufficient for achieving transient snowflakes but were unable to mitigate effects of disturbances on the configuration such as variations in the plasma inductance, edge current, and eddy currents in divertor structures. The first entirely closed-loop feedback control algorithm was developed and deployed on DIII-D [25]. The control scheme was capable of locating the SFD in real-time using a non-iterative X-point finder based upon series expansions of the magnetic field structure in the divertor region. A linear time-varying model relating changes in the divertor coil currents to changes in the snowflake geometry was used in-the-loop to compute the coil currents required for achieving a desired snowflake configuration. The algorithm was able to achieve stable plasma operations in a variety of configurations, including SFD-minus, SFD-plus, and near-exact snowflakes.

1.3. Paper outline

In this paper, we present a model-based, multiple-input-multiple-output (MIMO) algorithm that has been developed for real-time feedback control of snowflake divertor configurations on NSTX-U. The goal of this work is to develop an improved control scheme to address many of the limitations of the feedback algorithm as originally deployed on DIII-D. As identified in [25], desirable characteristics of an upgraded control system include capabilities for independent control of the locations of the primary and secondary X-points, higher fidelity modeling of the snowflake configuration response which includes the effects of plasma current redistribution on the positions of the two magnetic nulls, and model-based gain selection that minimizes the time required for gain optimization during plasma operations. The remainder of this paper is organized as follows: In Section 2, we derive a linear time-varying (LTV) model that describes the response of the snowflake geometric configuration to applied voltages on the divertor control coils. The primary components of the model are a set of coupled circuit equations describing the time-dynamics of the coil currents, a series approximation that models the response of an X-point position to changes in poloidal field structure, and a linearized model of the plasma response to changes in the poloidal field (PF) coil currents. In Section 3, we use the LTV model along with standard linear control synthesis techniques to design an optimal state feedback controller for the snowflake configuration. In Section 4, we present results of time-dependent, closed-loop simulations in which the controller is used to achieve and maintain a variety of SFD configurations of interest for future NSTX-U operations. Finally, in Section 5, we summarize our work and discuss plans for future control development.

2. System modeling for the snowflake divertor

The typical starting point for any control system design is the generation and validation of a model that describes the system dynamics of interest with sufficient accuracy. For this work, we seek a model that accurately describes the time-response of a set of geometric parameters that define the snowflake configuration to applied voltages on the divertor control coils. In particular, our goal is to derive a linear model in so-called state-space form,

$$\delta\dot{\mathbf{x}} = \mathbf{A}(t) \delta\mathbf{x} + \mathbf{B}(t) \delta\mathbf{v}, \quad (1a)$$

$$\delta\mathbf{y} = \mathbf{C}(t) \delta\mathbf{x} + \mathbf{D}(t) \delta\mathbf{v}, \quad (1b)$$

where \mathbf{v} is a vector that contains the values of the system actuator inputs, \mathbf{y} is a vector that contains measurements of the system outputs, and \mathbf{x} is a vector that contains a set of system parameters that uniquely define the dynamical state of the system. We note that the elements of \mathbf{x} are, in general, not directly measurable. For the SFD, it will be shown in Section 2.1 that the inputs \mathbf{v} are the coil voltages, the states \mathbf{x} are the coil currents, and the outputs \mathbf{y} are the snowflake shape descriptors. In (1a) and (1b), the symbol δ indicates that the aforementioned vectors are measured relative to

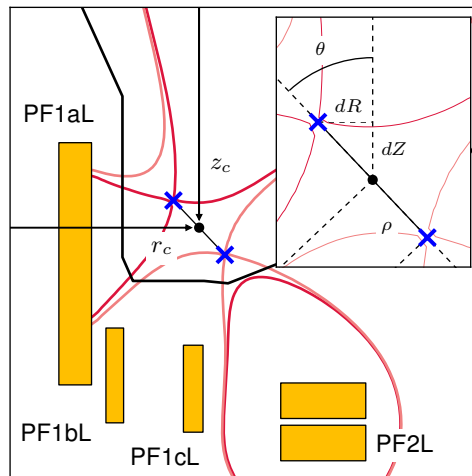


Figure 2. Illustration of the lower divertor on NSTX-U showing the limiter surface (black contour), the poloidal field coils available for snowflake divertor (SFD) control, and the shape parameters used to specify the geometry of the SFD magnetic configuration in the control system.

their values at some initial state. For the linear model of the snowflake configuration, the initial state will always be a set of PF coil currents and voltages that define a plasma equilibrium. Our primary task in this section is to identify the components of the (generally time-dependent) matrices $\mathbf{A}(t)$, $\mathbf{B}(t)$, $\mathbf{C}(t)$, and $\mathbf{D}(t)$ for the SFD system. Two common approaches to model identification are the data-based method, e.g. [26, 27], and the method which employs first-principles physics arguments, e.g. [28, 29]. In this paper, we choose to develop a linear model for the SFD based upon first-principles physics as the resulting model can easily be adapted to a variety of plasma scenarios and machine configurations. In particular, if the resulting model can be made sufficiently tractable, it is feasible for the control system to update the model parameters in real-time to account for the evolving plasma state. This capability enables the use of high-performance feedback control schemes such as real-time gain optimization and predictive control.

As actuators for the SFD configuration, the control algorithm presented in this work uses a set of three PF coils located in the divertor region. One of the notable aspects of the upgrade to NSTX-U was the installation of a new set of PF coils in the upper and lower divertor regions of the device, as depicted in Figure 2 for the lower divertor. The upgraded coil sets include an additional coil in each divertor region, relative to the coil configuration on NSTX prior to the upgrade, that were specifically designed for control of advanced divertor configurations such as the SFD. The additional coils provide improved shaping capabilities and are particularly important for maintaining the snowflake configuration at the current limits of the Ohmic solenoid (± 24 kA) during long-pulse inductive scenarios. As the PF1b coils will likely be unavailable during the first several years of NSTX-U operations, we have chosen to use the PF1a, PF1c, and PF2 coils as actuators for the snowflake configuration. In this paper, we develop a control

algorithm for SFD configurations in the lower divertor of NSTX-U (and therefore will be using the PF1aL, PF1cL, and PF2L coils for control). However, the algorithm is directly applicable to control of upper divertor snowflakes as the device is up-down symmetric. We also note that, since the model presented in this section is derived from first-principles physics arguments, the model as well as the control algorithm presented in Section 3 can likely be adapted for use on other devices with only minor modifications.

The duration of this section is organized as follows: In Section 2.1, we present the derivation of an equation of the form (1a) that describes the dynamics of the PF coils used to control the snowflake configuration on NSTX-U. The modeling framework presented in this section is widely used for tokamak magnetic control development and is discussed extensively elsewhere [30, 31]. We provide an outline of the modeling approach in this section as the results will be needed for design of the controller in Section 3. In Sections 2.2 and 2.3, we continue by deriving (1b) for the SFD system.

2.1. Linear MIMO model development for snowflake control

In this section, we present the development of a dynamical model for the SFD which will be used in Section 3 to design a model-based MIMO feedback controller for the configuration. In particular, we seek a model that accurately describes the dynamics that are relevant for control of the magnetic geometry in the divertor. As the axisymmetric plasma shape and divertor configuration are determined, in general, by the instantaneous values of all toroidal electric currents in the system, the primary dynamics of interest are the time responses of the currents in all toroidally axisymmetric conductors to applied voltages on the PF coils. To simplify the model used for control design, we include only the equations for the currents in divertor control coils and neglect currents induced in any nearby conducting structures such as the vacuum vessel. We will, however, include induced currents in a higher fidelity model used in Section 4 for system simulation and controller validation. In addition, we make the standard assumption that the plasma remains in force-balance on all time scales of interest for shape control.

To derive the equations which govern the divertor coil dynamics, we employ a standard formalism in the field of tokamak magnetic control in which the coils are modeled as inductively-coupled lumped parameter circuits,

$$\mathbf{M}_{\text{cc}}\dot{\mathbf{I}}_{\text{c}} + \dot{\Psi}_{\text{cp}} + \mathbf{R}_{\text{c}}\mathbf{I}_{\text{c}} = \mathbf{V}_{\text{c}}, \quad (2)$$

where \mathbf{M}_{cc} is the coil-to-coil mutual inductance matrix, \mathbf{R}_{c} is a diagonal matrix containing the resistances of the coil circuits, \mathbf{I}_{c} and \mathbf{V}_{c} are vectors containing the currents within and voltages applied to the divertor coils, respectively, and $\dot{\Psi}_{\text{cp}}$ represents the change in magnetic flux at the coils due to spatial redistribution of the plasma current. In general, the term $\dot{\Psi}_{\text{cp}}$ is a nonlinear function of the coil and plasma currents and must be determined by solving the free-boundary Grad-Shafranov problem. To obtain an LTV model of the form (1a) and (1b), we linearize $\dot{\Psi}_{\text{cp}}$ around a reference

plasma equilibrium as follows,

$$\mathbf{M}_{\text{cc}} \delta \dot{\mathbf{I}}_{\text{c}} + \left(\frac{\partial \Psi_{\text{cp}}}{\partial \mathbf{I}_{\text{c}}} \Big|_{\text{eq}(t)} \right) \delta \dot{\mathbf{I}}_{\text{c}} + \mathbf{R}_{\text{c}} \delta \mathbf{I}_{\text{c}} = \delta \mathbf{V}_{\text{c}}, \quad (3)$$

where we have shifted the coordinate system origin such that the coil currents \mathbf{I}_{c} and voltages \mathbf{V}_{c} are measured relative to their equilibrium values. The quantities $\delta \mathbf{I}_{\text{c}}$ and $\delta \mathbf{V}_{\text{c}}$ must remain small to ensure the validity of the linearization. By re-arranging the expression in (3), we find that,

$$\widehat{\mathbf{M}}(t) \delta \dot{\mathbf{I}}_{\text{c}} + \mathbf{R}_{\text{c}} \delta \mathbf{I}_{\text{c}} = \delta \mathbf{V}_{\text{c}}, \quad (4)$$

where we have defined,

$$\widehat{\mathbf{M}}(t) = \mathbf{M}_{\text{cc}} + \frac{\partial \Psi_{\text{cp}}}{\partial \mathbf{I}_{\text{c}}} \Big|_{\text{eq}(t)}, \quad (5)$$

which is a combination of a time-independent matrix \mathbf{M}_{cc} , which contains the vacuum mutual inductances between the divertor coils, and a matrix $\partial_{\mathbf{I}_{\text{c}}} \Psi_{\text{cp}}$, which represents an effective mutual inductance due to magnetic flux changes that result from a redistribution of the plasma current. The matrix $\partial_{\mathbf{I}_{\text{c}}} \Psi_{\text{cp}}$ is, in general, time-dependent as the response of the plasma may change as the discharge evolves. The expression (4) is simple to convert into the state-space form (1a),

$$\delta \dot{\mathbf{I}}_{\text{c}} = \mathbf{A}(t) \delta \mathbf{I}_{\text{c}} + \mathbf{B}(t) \delta \mathbf{V}_{\text{c}}, \quad (6)$$

where the matrices $\mathbf{A}(t)$ and $\mathbf{B}(t)$ are defined as follows,

$$\mathbf{A}(t) = - \left[\widehat{\mathbf{M}}(t) \right]^{-1} \mathbf{R}_{\text{c}}, \quad (7a)$$

$$\mathbf{B}(t) = \left[\widehat{\mathbf{M}}(t) \right]^{-1}, \quad (7b)$$

and the coil currents and voltages in vectors $\delta \mathbf{I}_{\text{c}}$ and $\delta \mathbf{V}_{\text{c}}$ are measured relative to their values in the equilibrium that was used to compute the response $\partial_{\mathbf{I}_{\text{c}}} \Psi_{\text{cp}}$. We discuss several approaches to computing this response matrix in Section 2.3.

To derive equation (1b), we must first define the output vector \mathbf{y} by identifying a suitable set of model outputs that we wish to control directly via the feedback algorithm. For the SFD, we choose to control the Cartesian coordinates of the snowflake centroid, denoted as (r_c, z_c) , as well as the parameters (dR, dZ) , which are the radial and vertical displacements of the primary X-point from the centroid. This choice of output vector is motivated by the realization in prior work that the control of certain divertor configurations, particularly the SFD-minus, is subject to significant ambiguity if the position of the primary X-point is not accounted for directly. In particular, there exist two distinct magnetic configurations that are classified as SFD-minus, one in which the secondary X-point lies in the high-field-side SOL, and another in which the secondary X-point lies in the low-field-side SOL. During previous experiments devoted to SFD control development, it was observed that the SFD-minus may transition unpredictably

between these two configurations if the control system is not specifically configured to prevent this behavior [25]. In this work, we directly control the location of the primary X-point, defined by the parameters (dR, dZ) , in order to remove this source of ambiguity. We also note that this parameterization of the SFD configuration is not unique. Two other shape parameters that will be referenced in this work (though not controlled directly) are the snowflake radius ρ , defined as half the distance between the two X-points, and angle θ , defined as the angular orientation of the primary X-point relative to the vertical direction. An illustration of all snowflake shape descriptors used in this paper is provided in Figure 2.

After selecting the set of snowflake shape descriptors, we can define the output matrix $\mathbf{C}(t)$ in (1b) as follows,

$$\mathbf{C}(t) = \begin{bmatrix} \partial_{\mathbf{I}_c} r_c \\ \partial_{\mathbf{I}_c} z_c \\ \partial_{\mathbf{I}_c} dR \\ \partial_{\mathbf{I}_c} dZ \end{bmatrix}, \quad (8)$$

where the operator $\partial_{\mathbf{I}_c}$ denotes partial differentiation with respect to each of the control coil currents. Each row of $\mathbf{C}(t)$ can be computed separately as follows,

$$\partial_{\mathbf{I}_c} r_c = \partial_{\mathbf{B}} r_c (\partial_{\mathbf{I}_c} \mathbf{B} + \partial_{\mathbf{J}} \mathbf{B} \cdot \partial_{\mathbf{I}_c} \mathbf{J}), \quad (9a)$$

$$\partial_{\mathbf{I}_c} z_c = \partial_{\mathbf{B}} z_c (\partial_{\mathbf{I}_c} \mathbf{B} + \partial_{\mathbf{J}} \mathbf{B} \cdot \partial_{\mathbf{I}_c} \mathbf{J}), \quad (9b)$$

$$\partial_{\mathbf{I}_c} dR = \partial_{\mathbf{B}} dR (\partial_{\mathbf{I}_c} \mathbf{B} + \partial_{\mathbf{J}} \mathbf{B} \cdot \partial_{\mathbf{I}_c} \mathbf{J}), \quad (9c)$$

$$\partial_{\mathbf{I}_c} dZ = \partial_{\mathbf{B}} dZ (\partial_{\mathbf{I}_c} \mathbf{B} + \partial_{\mathbf{J}} \mathbf{B} \cdot \partial_{\mathbf{I}_c} \mathbf{J}). \quad (9d)$$

In (9a) through (9d), the first terms that contain partial derivatives $\partial_{\mathbf{B}}$ represent the linearized responses of the snowflake shape descriptors to changes in the poloidal magnetic field. The terms in parentheses that contain partial derivatives $\partial_{\mathbf{I}_c}$ represent the linearized response of the poloidal magnetic field to changes in the control coil currents. This response consists of two distinct components: The term $\partial_{\mathbf{I}_c} \mathbf{B}$ represents the direct response of the field to coil current changes and is independent of the plasma configuration. The elements of $\partial_{\mathbf{I}_c} \mathbf{B}$ can be computed from the mutual inductances between the coils and a spatial grid of points at which the field is evaluated. In (9a) through (9d), the term $\partial_{\mathbf{J}} \mathbf{B}$ represents the linear change in poloidal field that results from a redistribution of the plasma current (which is caused by changing the coil currents), while $\partial_{\mathbf{I}_c} \mathbf{J}$ quantifies the change in plasma current distribution due to the coils. These values must be computed from an assumed model of the plasma response. We discuss several methods for performing this calculation in Section 2.3.

2.2. Modeling of the X-point position response

In order to determine analytical formulas for the linearized responses of the snowflake shape descriptors to changes in the poloidal field, we compute the response of a standard first-order null and then use this expression to determine the responses of the two nulls

of the SFD configuration. One method for obtaining an analytical formula for the X-point response is to first approximate the field structure in the vicinity of the null by solving the toroidal component of Ampère's law,

$$(r_0 + x) \frac{\partial}{\partial x} \left(\frac{1}{r_0 + x} \frac{\partial \psi}{\partial x} \right) + \frac{\partial^2 \psi}{\partial v^2} = 0, \quad (10)$$

where $\psi(x, z)$ is the poloidal magnetic flux function, x is the radial coordinate relative to the position r_0 , and v is the vertical coordinate relative to the position z_0 . The coordinates (r_0, z_0) can be chosen arbitrarily subject to the constraint that this point lies close to the X-point. The flux function is related to the radial, B_r , and vertical, B_z , components of the magnetic field through the following relations,

$$B_r = -\frac{1}{r_0 + x} \frac{\partial \psi}{\partial v}, \quad (11a)$$

$$B_z = \frac{1}{r_0 + x} \frac{\partial \psi}{\partial x}. \quad (11b)$$

In (10), we have assumed that the current density in the divertor region is small and therefore can be neglected. As shown in [32] for the case of a second-order null, finite current density effects can be included in the derivation if desired. However, we have found that the simplifying assumption of zero toroidal current provides an adequate model for controller design.

We next expand the flux function as a series to second-order,

$$\psi(x, v) = l_1 x + l_2 v + q_1 x^2 + 2q_2 x v + q_3 v^2, \quad (12)$$

where we have neglected the constant term as it does not contribute to the components of the poloidal field. Upon substituting (12) into (10) and equating the constant term to zero, we obtain one constraint on the expansion coefficients that must be satisfied for any field configuration,

$$l_1 = 2r_0 (q_1 + q_3). \quad (13)$$

Furthermore, by substituting (12) into (11a) and (11b) and employing (13) to eliminate the l_1 coefficient, we obtain formulas for the poloidal field components B_r and B_z ,

$$B_r = -\frac{1}{r_0 + x} (l_2 + 2q_2 x + 2q_3 v), \quad (14a)$$

$$B_z = \frac{1}{r_0 + x} (2(r_0 + x)q_1 + 2q_2 v + 2q_3 r_0), \quad (14b)$$

which are linear functions of the l_2, q_1, q_2, q_3 series coefficients. These coefficients can be determined provided that the values of B_r and B_z at two points in the vicinity of the X-point are known. During plasma operations, the magnetic field values can typically be obtained from a real-time equilibrium reconstruction algorithm.

After computing the expansion coefficients, we may calculate the (r, z) coordinates of the X-point by setting $B_r = B_z = 0$ and solving the resulting equations for the radial

and vertical coordinates. We obtain the following,

$$r_x = r_0 + \frac{l_2 q_2 - l_1 q_3}{2(q_1 q_3 - q_2^2)}, \quad (15a)$$

$$z_x = z_0 + \frac{l_2 q_1 - l_1 q_2}{2(q_2^2 - q_1 q_3)}. \quad (15b)$$

The X-point coordinates (15a) and (15b) can be easily differentiated to determine the desired response of the X-point position to changes in the poloidal field. Differentiating with the chain rule results in the following,

$$\partial_{\mathbf{B}} r_x = \partial_{\mathbf{c}} r_x \cdot \partial_{\mathbf{B}} \mathbf{c} \quad (16a)$$

$$\partial_{\mathbf{B}} z_x = \partial_{\mathbf{c}} z_x \cdot \partial_{\mathbf{B}} \mathbf{c} \quad (16b)$$

where the operator $\partial_{\mathbf{c}}$ denotes partial differentiation with respect to the expansion coefficients. The terms $\partial_{\mathbf{c}} r_x$ and $\partial_{\mathbf{c}} z_x$ are computed directly from (15a) and (15b), while $\partial_{\mathbf{B}} \mathbf{c}$ is the inverse of the matrix that was used to compute the expansion coefficients from the field measurements.

In order to obtain the response of the SFD configuration to changes in the poloidal magnetic field, we first compute the individual response of each X-point, located at the coordinates (r_{x_1}, z_{x_1}) and (r_{x_2}, z_{x_2}) , respectively. The responses of the snowflake shape descriptors, as required in (9a) through (9d), are then computed as follows,

$$\partial_{\mathbf{B}} r_c = (\partial_{\mathbf{c}} r_{x_1} + \partial_{\mathbf{c}} r_{x_2}) / 2, \quad (17a)$$

$$\partial_{\mathbf{B}} z_c = (\partial_{\mathbf{c}} z_{x_1} + \partial_{\mathbf{c}} z_{x_2}) / 2, \quad (17b)$$

$$\partial_{\mathbf{B}} dR = (\partial_{\mathbf{c}} r_{x_1} - \partial_{\mathbf{c}} r_{x_2}) / 2, \quad (17c)$$

$$\partial_{\mathbf{B}} dZ = (\partial_{\mathbf{c}} z_{x_1} - \partial_{\mathbf{c}} z_{x_2}) / 2. \quad (17d)$$

2.3. Rigid plasma response modeling

The remaining task in the SFD modeling procedure is to compute the derivatives that quantify the linear response of flux and field to changes in the distribution of toroidal plasma current. In particular, we require the matrix $\partial_{\mathbf{I}_c} \Psi_{\mathbf{cP}}$ in (3) as well as the terms $\partial_{\mathbf{J}} \mathbf{B}$ and $\partial_{\mathbf{I}_c} \mathbf{J}$ in (9a) through (9d). The approach that is taken to obtaining these derivatives can be better understood by first decomposing $\partial_{\mathbf{I}_c} \Psi_{\mathbf{cP}}$ as follows,

$$\frac{\partial \Psi_{\mathbf{cP}}}{\partial \mathbf{I}_c} = \frac{\partial \Psi_{\mathbf{cP}}}{\partial \boldsymbol{\xi}_r} \frac{\partial \boldsymbol{\xi}_r}{\partial \mathbf{I}_c} + \frac{\partial \Psi_{\mathbf{cP}}}{\partial \boldsymbol{\xi}_z} \frac{\partial \boldsymbol{\xi}_z}{\partial \mathbf{I}_c}, \quad (18)$$

where $\boldsymbol{\xi}_r$ and $\boldsymbol{\xi}_z$ are plasma fluid element displacement vectors in the radial and vertical directions, respectively. The evaluation of the required derivatives therefore necessitates the calculation of $\partial_{\mathbf{I}_c} \boldsymbol{\xi}_r$ and $\partial_{\mathbf{I}_c} \boldsymbol{\xi}_z$, the response of the plasma fluid elements to changes in the coil currents.

One of two modeling formalisms is typically employed for this purpose: (1) Under the rigid plasma assumption, the plasma current distribution is constrained to move rigidly in the radial and vertical directions such that the relative distribution of plasma

current in the poloidal plane remains constant. The response of the plasma is therefore completely defined by the responses of r_C and z_C , the radial and vertical coordinates of the plasma current centroid (not to be confused with r_c and z_c , the coordinates of the SFD centroid). (2) In contrast to the rigid plasma constraint, the plasma fluid elements may be allowed to move independently in both the radial and vertical directions. The total plasma response is therefore determined by the individual displacements of all fluid elements. This response model is often referred to as the nonrigid or perturbed equilibrium model as the model requires the solution of a perturbed form of the Grad-Shafranov equation. It should be emphasized that, in both the rigid and nonrigid models, the assumption is made that all plasma displacements occur in a manner that conserves either a global or local form of force-balance. Further discussion of both rigid [26, 31] and nonrigid [33, 34] response models can be found in the relevant literature.

For SFD control development, we choose to model the plasma as a rigid body due to the relative simplicity of this approach. Our problem is therefore reduced from the calculation of $\partial_{\mathbf{I}_c}\boldsymbol{\xi}_r$ and $\partial_{\mathbf{I}_c}\boldsymbol{\xi}_z$ to the calculation of $\partial_{\mathbf{I}_c}r_C$ and $\partial_{\mathbf{I}_c}z_C$. The response matrices are then used to construct the remaining unknown derivatives in (3) and (9a) through (9d). For details of this procedure, the reader may refer to Appendix A.

3. Controller design for the snowflake divertor

In this section, we use the linear model developed in Section 2 to design a feedback controller for the SFD configuration on NSTX-U. The resulting control algorithm is constructed from three primary components: (1) a feedforward gain matrix, which is used to estimate the PF coil voltages and currents required to achieve the desired SFD configuration, (2) a full-state feedback control law, which generates a set of voltage commands for the PF coils that is proportional to the error between the target and present values of the coil currents, and (3) an integral feedback term, which improves tracking of the reference SFD configuration in the presence of modeling uncertainties and system disturbances by minimizing the integrated error between the desired and present values of the snowflake parameters. In Section 3.1, we provide an overview of the control scheme and derive the control law that is used for generating appropriate voltage commands for the PF coils. In Section 3.2, we compute feedback gains for the control system using a standard control design technique known as the linear quadratic regulator. Finally, in Section 3.3, we describe how the state feedback control scheme can be augmented with integral action to ensure proper tracking of the reference snowflake configuration. A block diagram illustrating the major components of the control system and their interconnections is provided in Figure 3.

3.1. State feedback with reference tracking

The objective of the control algorithm is to command the system to a desired state vector \mathbf{x}_d that corresponds to a set of desired system outputs \mathbf{y}_d . In the particular case

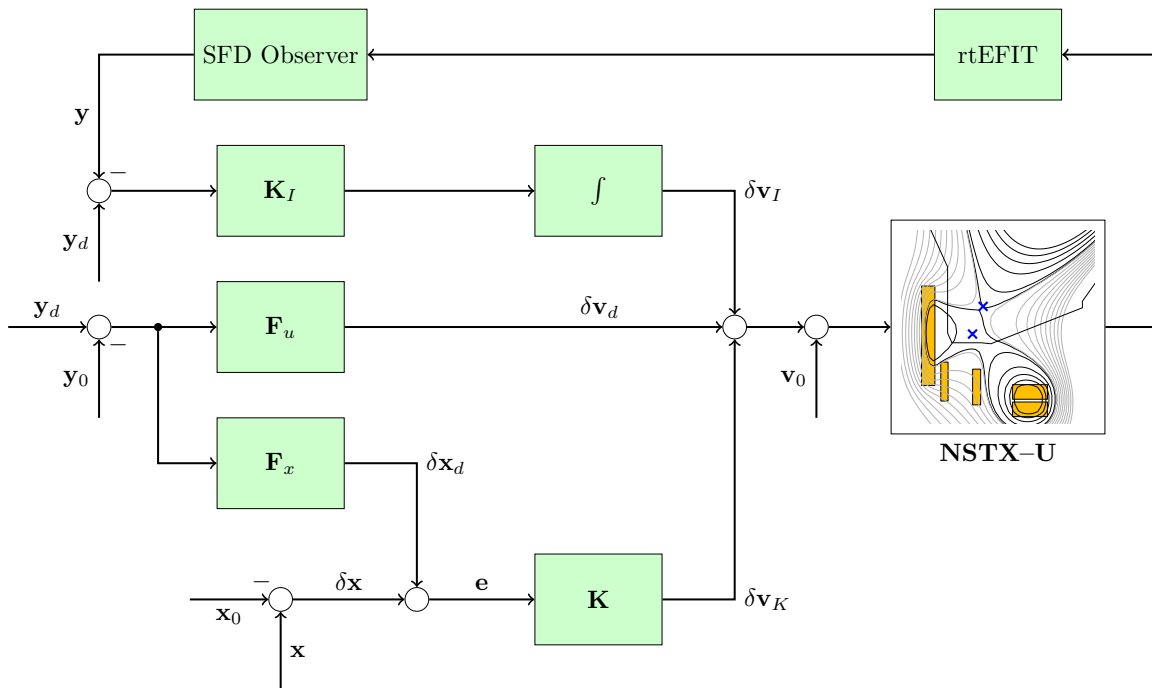


Figure 3. Block diagram depicting the data flow through the snowflake divertor control system on NSTX-U. The control law is the sum of three primary components: (1) a feedforward term with gain matrices \mathbf{F}_u and \mathbf{F}_x , (2) a state-feedback control law for obtaining the desired PF coil currents with optimal gain matrix \mathbf{K} computed by the LQR algorithm, and (3) an integral term with gain matrix \mathbf{K}_I for achieving zero steady-state error in the snowflake shape descriptors.

of the SFD, the desired states are the coil currents and the desired outputs are a set of shape parameters which define the desired SFD configuration. The goal of the control algorithm should therefore be to minimize the state error $\mathbf{e} = \mathbf{x} - \mathbf{x}_d$, the difference between the present and desired values of the state vector (coil currents). Using (1a), the error dynamics can be computed as,

$$\dot{\mathbf{e}} = \mathbf{A}(t)\mathbf{e} + \mathbf{B}(t)\mathbf{u}, \quad (19)$$

where $\mathbf{u} = \mathbf{v} - \mathbf{v}_d$, the difference between the present and desired values of the input voltage vector. Using (19), we can then design a state feedback controller of the following form,

$$\mathbf{u} = -\mathbf{K}(t)\mathbf{e}, \quad (20)$$

where \mathbf{K} is a matrix of feedback gains with dimension $m \times n$, where m is the number of inputs and n is the number of states. The product of \mathbf{K} and \mathbf{e} shall therefore produce a set of appropriate voltages \mathbf{u} for the coils which will result in a minimum state error. Using (20), the total input to the system is as follows,

$$\mathbf{v} = \mathbf{K}(t)(\mathbf{x}_d - \mathbf{x}) + \mathbf{v}_d. \quad (21)$$

The remaining task is to compute the desired state vector \mathbf{x}_d and the desired input vector \mathbf{v}_d , which we shall refer to hereafter as the feedforward state (coil current) and input (voltage) vectors. This is accomplished as follows: When the system reaches a steady-state ($\dot{\mathbf{x}} = 0$), the system output vector \mathbf{y} should equal the desired value \mathbf{y}_d . Using (1a) and (1b), the following conditions are therefore satisfied,

$$0 = \mathbf{A}(t)\mathbf{x}_d + \mathbf{B}(t)\mathbf{v}_d, \quad (22a)$$

$$\mathbf{y}_d = \mathbf{C}(t)\mathbf{x}_d, \quad (22b)$$

where we have assumed that $\mathbf{D}(t) = 0$, as is true for the SFD system. Upon solving (22a) and (22b), we obtain,

$$\mathbf{x}_d = \mathbf{C}^\dagger(t) \mathbf{y}_d, \quad (23a)$$

$$\mathbf{v}_d = -\mathbf{B}^{-1}(t)\mathbf{A}(t)\mathbf{C}^\dagger(t) \mathbf{y}_d, \quad (23b)$$

where the symbol \dagger denotes the matrix pseudoinverse. The expressions (23a) and (23b) are then used to define the following feedforward gain matrices,

$$\mathbf{F}_x = \mathbf{C}^\dagger(t), \quad (24a)$$

$$\mathbf{F}_u = -\mathbf{B}^{-1}(t)\mathbf{A}(t)\mathbf{C}^\dagger(t), \quad (24b)$$

where \mathbf{F}_x is the feedforward state matrix and \mathbf{F}_u is the feedforward input matrix.

Since the linearized model (1a) and (1b) is only valid for small perturbations about the defining equilibrium, it should be emphasized that all vector quantities in this section are measured relative to their equilibrium values. The inputs and outputs to the control algorithm must therefore be measured in the perturbed coordinate system by addition or subtraction of the corresponding equilibrium quantities. For the sake of simplicity, we have refrained from expressing (19) through (24b) in perturbed coordinates. However, the required coordinate system shifts are depicted explicitly in Figure 3, where $(\mathbf{v}_0, \mathbf{x}_0, \mathbf{y}_0)$ are the equilibrium values of the input, state, and output vectors, respectively. As the model (1a) and (1b) is time-varying, we also note that the control system parameters, such as the feedforward and feedback gain matrices, should be updated periodically to account for changes in the system dynamics.

3.2. LQR optimal control design

The control law as formulated in (20) and (21) requires that a matrix of feedback control gains \mathbf{K} be computed which converts a vector of state errors to a vector of coil voltage commands. For this purpose, we employ a common technique in control system design known as the linear quadratic regulator (LQR). The algorithm computes a matrix of feedback gains \mathbf{K} which minimize the following quadratic cost function,

$$\mathcal{J} = \int_0^\infty (\mathbf{e}^\top \mathbf{Q} \mathbf{e} + \mathbf{u}^\top \mathbf{R} \mathbf{u}) dt, \quad (25)$$

where \mathbf{e} and \mathbf{u} are the error and input vectors, respectively, as defined in the previous section, and \mathbf{Q} and \mathbf{R} are symmetric, positive-definite weighting matrices with entries

that are defined by the control designer. It can be shown that the optimal gain matrix \mathbf{K} which minimizes (25) is given by,

$$\mathbf{K} = \mathbf{R}^{-1}\mathbf{B}^T\mathbf{P}, \quad (26)$$

where \mathbf{P} is a symmetric, positive-definite matrix that satisfies the matrix equation,

$$\mathbf{A}^T\mathbf{P} + \mathbf{P}\mathbf{A} - \mathbf{P}\mathbf{B}\mathbf{R}^{-1}\mathbf{B}^T\mathbf{P} + \mathbf{Q} = 0. \quad (27)$$

This equation is known as the algebraic Riccati equation and is solved iteratively using standard algorithms in commercial software packages such as MATLAB. More details pertaining to state feedback control design and the LQR algorithm may be found in standard reference works [35, 36, 37].

3.3. Integral action

It is well known that the control system as formulated by the feedback law (21) will often perform poorly when attempting to track nonzero reference trajectories for the system outputs. The source of this deficiency is the absence of a term in (21) that is dependent upon the errors between the measured and desired system outputs. Rather, output tracking is accomplished indirectly by computing the feedforward currents and voltages in (23a) and (23b) at which the system outputs assume their desired values. This approach therefore requires a highly accurate model of the system dynamics and is unable to compensate for modeling uncertainties or system disturbances. A commonly-employed remedy is to augment the system state vector with a term that depends explicitly on the output tracking errors [38]. In particular, we may introduce a new state \mathbf{z} , which is defined as the integral of the error between the desired and measured system outputs,

$$\mathbf{z} = \int_0^t (\mathbf{y}_d - \mathbf{y}) d\tau. \quad (28)$$

The dynamics for the augmented system are as follows,

$$\frac{d}{dt} \begin{bmatrix} \mathbf{x} \\ \mathbf{z} \end{bmatrix} = \begin{bmatrix} \mathbf{A}(t) & 0 \\ -\mathbf{C}(t) & 0 \end{bmatrix} \begin{bmatrix} \mathbf{x} \\ \mathbf{z} \end{bmatrix} + \begin{bmatrix} \mathbf{B}(t) \\ 0 \end{bmatrix} \mathbf{v} + \begin{bmatrix} 0 \\ \mathbf{I} \end{bmatrix} \mathbf{y}_d, \quad (29)$$

where \mathbf{I} is the identity matrix. The feedback control law for the augmented system can therefore be expressed as,

$$\mathbf{v} = \mathbf{K}(t) (\mathbf{x}_d - \mathbf{x}) + \mathbf{K}_I(t) \mathbf{z} + \mathbf{v}_d. \quad (30)$$

where \mathbf{K} is the matrix of state feedback gains as computed in Section 3.2 and \mathbf{K}_I is an additional set of gains for the error integrals. We note that, if the closed-loop system is stable, there will exist a steady-state condition at which $\dot{\mathbf{z}} = 0$ and $\mathbf{y} = \mathbf{y}_d$. The use of integral action therefore guarantees zero error in steady-state between the measured and desired values of the system outputs.

The remaining task of the control design is to compute the matrix \mathbf{K}_I of integral gains. For this purpose, the error vector \mathbf{e} in the cost function (25) may be replaced by the augmented error vector \mathbf{e}^* , defined as,

$$\mathbf{e}^* = \begin{bmatrix} \mathbf{e} \\ \mathbf{z} \end{bmatrix}. \quad (31)$$

We may then proceed with a standard LQR control design to compute both the state feedback gain matrix \mathbf{K} as well as the integral gain matrix \mathbf{K}_I . As inputs to the cost function for the LQR design, we define the weighting matrices to be $\mathbf{Q} = \text{diag}(10^{-4} \cdot \mathbf{I}_{3 \times 3}, 10^{10} \cdot \mathbf{I}_{4 \times 4})$ and $\mathbf{R} = \rho \mathbf{I}_{3 \times 3}$, where $\rho = 1$ but can be varied if necessary to achieve the desired transient response. The diagonal elements of the matrix \mathbf{Q} were chosen to provide equal weighting in the cost function to a coil current error of 100A and to an instantaneous error in the snowflake parameters of 5 cm.

3.4. Equilibrium reconstruction and SFD shape observer

We conclude our discussion of the control algorithm design by noting that several additional components, while not the focus of this paper, are required by the control system, namely, the rtEFIT algorithm for equilibrium reconstruction [39] and the SFD shape observer for identifying the snowflake configuration during plasma operations. The rtEFIT algorithm computes in real-time a realistic solution to the plasma force-balance relation that is constrained by measurements of flux and field from a variety of magnetic sensors on the device. In particular, rtEFIT provides a reasonably accurate estimation of the plasma boundary location to enable precise control of the plasma cross-sectional shape. The rtEFIT algorithm was used extensively on NSTX [40] and NSTX-U [41] in conjunction with the ISOFLUX shape control algorithm for plasma boundary and divertor configuration control. The SFD shape observer is designed to operate in series with rtEFIT and is used for determining the locations of the two X-points that comprise the snowflake configuration. The shape observer employs an algorithm similar to that derived in Section 2.2 to approximate the field topology in the divertor region given the field measurements (B_r, B_z) at three points. The X-point locations of the SFD can then be found by solving for the (r, z) coordinates at which $B_r = B_z = 0$. The observer algorithm was developed as a supplement to the iterative procedure used by rtEFIT for locating a first-order null of the standard divertor configuration. Details of the algorithm used by the SFD shape observer may be found in [25].

4. Feedback control simulation results

4.1. Simulation overview

In order to validate the performance of the proposed controller for the SFD configuration, a control system simulator was developed for NSTX-U that evolves the linear dynamics of the conductor currents simultaneously with the plasma force-balance as defined by

the free-boundary Grad-Shafranov equation. For simulation of the conductor current dynamics, we model all toroidally-axisymmetric conductors as inductively-coupled lumped parameter circuits in a manner analogous to that which was used in Section 2.1 for modeling of the divertor control coils. The relevant equations for the combined system of conductors are as follows,

$$\mathbf{M}_{cc} \dot{\mathbf{I}}_c + \mathbf{M}_{cv} \dot{\mathbf{I}}_v + \dot{\Psi}_{cp} + \mathbf{R}_c \mathbf{I}_c = \mathbf{V}_c, \quad (32a)$$

$$\mathbf{M}_{vc} \dot{\mathbf{I}}_c + \mathbf{M}_{vv} \dot{\mathbf{I}}_v + \dot{\Psi}_{vp} + \mathbf{R}_v \mathbf{I}_v = 0, \quad (32b)$$

where (32a) describes the dynamics of the currents in the PF coils and (32b) describes the dynamics of the currents in passive conducting structures such as the vacuum vessel and passive stabilization plates. Figure 4 provides a cross-sectional view of the device that depicts all axisymmetric conductors which were included in the simulations. The mutual inductances between coils and passive conductors were computed analytically, while the resistances of the passive conductors were determined by identifying values that produced good agreement between predicted and measured magnetic diagnostic signals for data obtained during vacuum-only test shots of the poloidal field coils. No attempt was made to optimize the resistance calculations, although we note that the development of methods for computing best-fit vessel resistances for NSTX-U is ongoing. In addition to the linear models of the conductor current dynamics, a free-boundary Grad-Shafranov equilibrium solver was developed to evolve the plasma boundary and divertor configuration given the prescribed values of currents in all coils and passive conductors. The plasma profiles $p'(\psi)$ and $F(\psi)F'(\psi)$ were defined by cubic spline curves with coefficients which were automatically updated during simulations to keep the scalar parameters I_p , β_p , and l_i approximately constant. All code and related infrastructure for the simulations was implemented in the MATLAB/Simulink environment [42].

To be used as an initial condition for the simulation, a snowflake equilibrium was designed by modifying the reconstructed equilibrium from a lower single null (LSN), H-mode plasma discharge on NSTX-U (specifically, discharge 204118 at 509 ms) with plasma parameters $I_p = 1$ MA, $\beta_p = 1.0$, and $l_i = 0.6$. As inputs to the free-boundary Grad-Shafranov solver used for the equilibrium design, the currents in the PF coils used for control of the upper X-point position (PF1aU and PF2U), upper boundary squareness (PF3U), and outer gap (PF5) were locked at their LSN equilibrium values. It was determined through trial-and-error that the LSN plasma boundary was not compatible with some desired SFD configurations, particularly near-exact snowflakes, due to the relatively long divertor leg connecting the primary X-point to the outer strike point. This issue was addressed by decreasing the current in the PF3L coil by approximately 1.5 kA in order to increase the lower boundary squareness and reduce the primary X-point height. The currents in the PF2L, PF1cL, and PF1aL coils were then adjusted to generate the desired SFD configuration. The coil current values for all active coils, as well as the plasma boundary shapes for the initial LSN equilibrium and the designed SFD equilibrium, are shown in Figure 4.

During the SFD control simulations, all active PF coils were operated in closed-

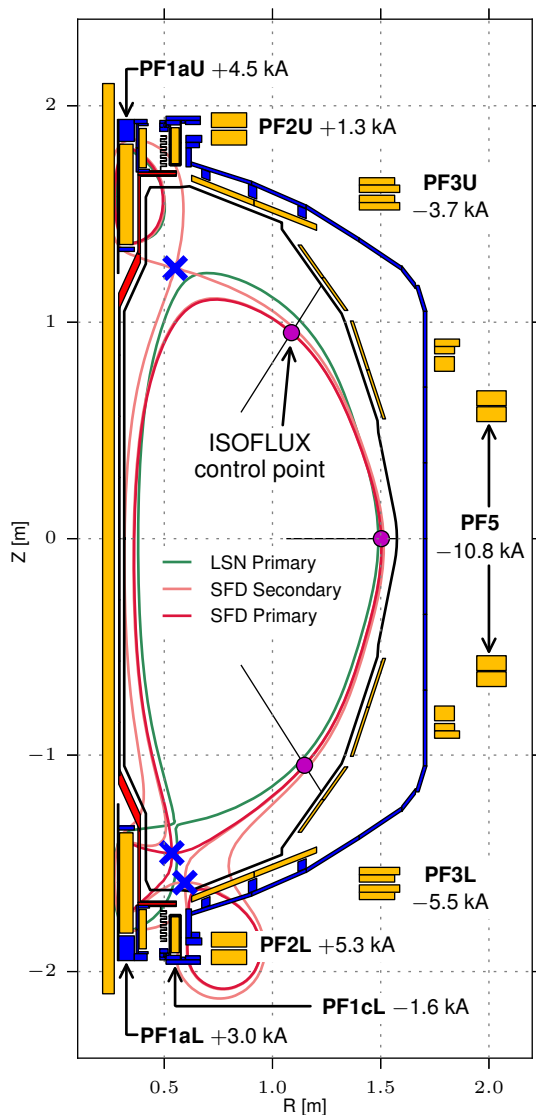


Figure 4. Cross-sectional view of NSTX-U depicting the toroidally-axisymmetric conductors (e.g. poloidal field coils and vacuum vessel) that were modeled in the control system simulator. Inside the vacuum vessel are plotted the separatrices from the initial lower single null discharge used for equilibrium design and the resulting snowflake divertor (SFD) equilibrium. Also shown are the coil currents for all active coils in the SFD equilibrium and the ISOFUX control points which were used for control of the plasma boundary shape during simulations.

loop by one of two control algorithms: Voltage commands for the PF1aL, PF1cL, and PF2L coils were computed by the SFD control algorithm as described in this paper. The other active PF coils were operated under ISOFUX control with the goal of maintaining the plasma boundary shape and upper X-point position while the geometry of the SFD configuration was modified by the lower divertor coils. The ISOFUX algorithm regulates the plasma boundary shape by minimizing the errors between the fluxes at control points on the desired boundary and the flux at the X-point on the

separatrix. The radial and vertical coordinates of the upper X-point are controlled directly by the divertor coils. The ISOFLUX algorithm is primarily single-input-single-output and uses a proportional-integral-derivative (PID) control law to compute voltage commands for the coils. For the simulations discussed in this paper, the PID gains were tuned empirically in simulations to provide reasonably good transient response and small steady-state error.

To conclude our overview of the control system simulator, we provide a brief description of the approximate sequence of events which occurs during each simulation: A set of voltage commands for the PF coils is first computed using either the ISOFLUX or SFD control algorithms. Given the values of the coil voltages, (32a) and (32b) are integrated forward in-time to determine the instantaneous currents in all toroidally-axisymmetric conductors. The magnetic flux on the grid is then updated by solving the free-boundary Grad-Shafranov problem for the plasma equilibrium that is consistent with the instantaneous conductor currents and the target values for I_p , β_p , and l_i . A set of plasma shape parameters, such as control points fluxes and snowflake X-point positions, is then computed for input to the control algorithms during the next time-step. We note that the system (32a) and (32b) generally has one unstable eigenvalue corresponding to the well-known axisymmetric vertical instability [43]. For the purposes of SFD control validation, we artificially stabilize the system by negating the unstable eigenvalue. This choice is akin to assuming that the plasma vertical position is stabilized by a separate control loop as is done on NSTX-U.

4.2. Simulation results

The shape control simulator was used to validate the performance of the proposed SFD control algorithm with particular emphasis on the demonstration of controlled operations in and transitions between a variety of divertor configurations. To this end, we studied the controller performance in three distinct scenarios: (1) Transition from low-field-side to high-field-side SFD-minus (as discussed in detail in Section 2) at constant X-point separation, (2) scan of the X-point separation from a quasi-snowflake to a near-perfect SFD in the SFD-plus configuration, and (3) scan of the X-point separation from a quasi-snowflake to a near-perfect SFD in the SFD-minus configuration. We use the term quasi-snowflake to refer qualitatively to any configuration in which there are two distinct nulls that are separated by a reasonable distance. The three simulation scenarios, when taken together, demonstrate that the control algorithm is capable of achieving a large range of SFD configurations on NSTX-U.

Figure 5 illustrates the results of the simulations by displaying a series of equilibria for each scenario. In each case, time is measured relative to the time for the equilibrium in the top-left frame, which is taken to be $t = 0$. Also plotted in dashed lines for each scenario are the desired X-point trajectories. In Figure 5a, we depict the results of the scan of the snowflake angular orientation at constant X-point separation. At the initial time, the divertor configuration is a SFD-minus with the secondary X-point in

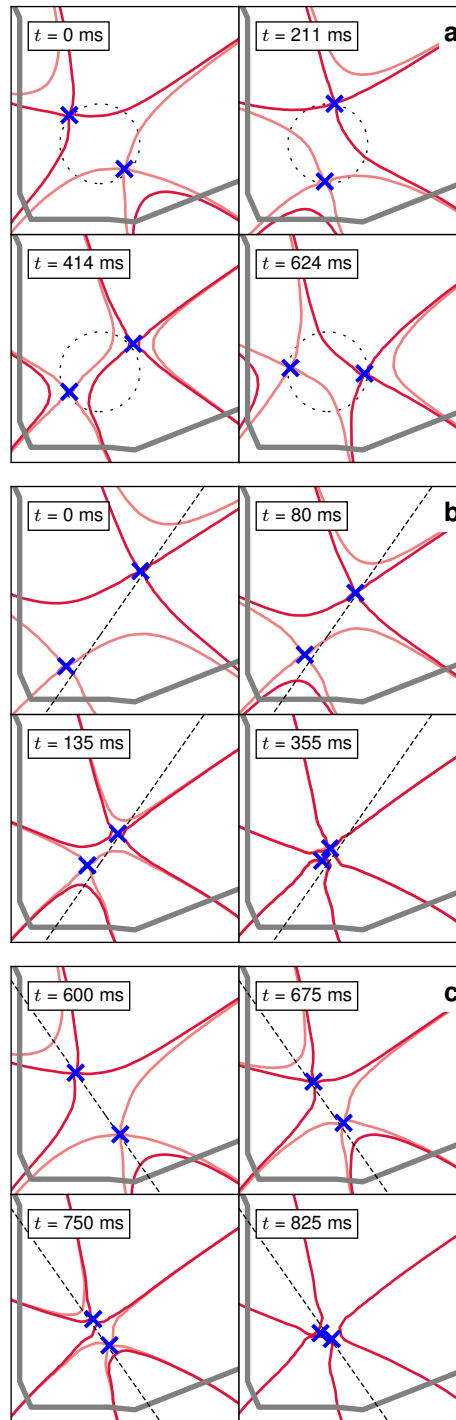


Figure 5. Closed-loop simulation results depicting the primary and secondary X-point trajectories during controlled scans of the SFD configuration on NSTX-U. Three scenarios are depicted: (a) scan of the angular orientation at constant X-point separation, (b) scan of the X-point separation at constant orientation in SFD-plus, and (c) scan of the X-point separation at constant orientation in SFD-minus. The algorithm enables controlled operations on NSTX-U in a wide range of divertor configurations.

the SOL on the low-field-side. As time progresses, the control algorithm rotates the configuration clockwise around the dashed circle. By $t = 624$ ms, the configuration has converted to a SFD-minus with the secondary X-point in the SOL on the high-field-side. Since the algorithm enables controlled transition between the two variants of the SFD-minus configuration, the control system provides a mechanism for rectifying scenarios in which the configuration may convert unpredictably from one configuration to the other. In Figure 5b and 5c, we depict the results of controlled scans of the X-point separation at constant angular orientation. In both figures, the dashed lines indicate the desired orientation that the control system should attempt to achieve as the two X-points approach each other. It is seen that control system is capable of converting both SFD-plus and SFD-minus configurations to near-perfect snowflakes while adhering quite closely to the desired orientations.

In Figures 6 and 7, we display time traces of the snowflake shape parameters as well as the divertor coil currents and voltages for the scenario depicted in Figure 5a (snowflake angle scan). In Figure 6, the top row illustrates the time histories of the three parameters that were controlled directly in the simulation, namely, the radial coordinate of the snowflake centroid and the radial and vertical displacements of the primary X-point from the centroid. In all simulations for this paper, the vertical coordinate of the centroid was uncontrolled and allowed to float to a natural position. It is worth noting that in scenarios with three parameters controlled, the output matrix (8) is fully-invertible as the number of controlled parameters does not exceed the number of actuators., and we should therefore be able to achieve desired (r_c, dR, dZ) with a well-designed controller. This was the case for the simulations presented in this paper, as can be seen for the angle scan in Figure 6. Investigation of underactuated scenarios in which additional parameters are controlled will be the subject of future work. The second row of Figure 6 also depicts the time histories of the snowflake radius and angle. These parameters were indirectly controlled by the parameters (dR, dZ) . Furthermore, Figure 7 depicts the coil voltages and currents for the PF1aL, PF1cL, and PF2L coils during the scan of the SFD orientation. We emphasize that both the currents and voltages remain well-within their operational limits throughout the simulation. The currents and voltages for the other two scenarios exhibit similar behavior and are therefore not shown.

5. Discussion and conclusion

In this paper, we have presented the design and validation of a feedback algorithm for control of snowflake divertor configurations on NSTX-U. A higher fidelity model of the snowflake configuration response to applied voltages on the divertor control coils was derived that accounts for additional affects such as the primary X-point tracking and the effects of plasma current redistribution. The model was then used to design a model-based controller for the SFD configuration using a modern multivariable control design technique known as the linear quadratic regulator. A control system simulator was developed that evolves the currents in coils and passive structures simultaneously

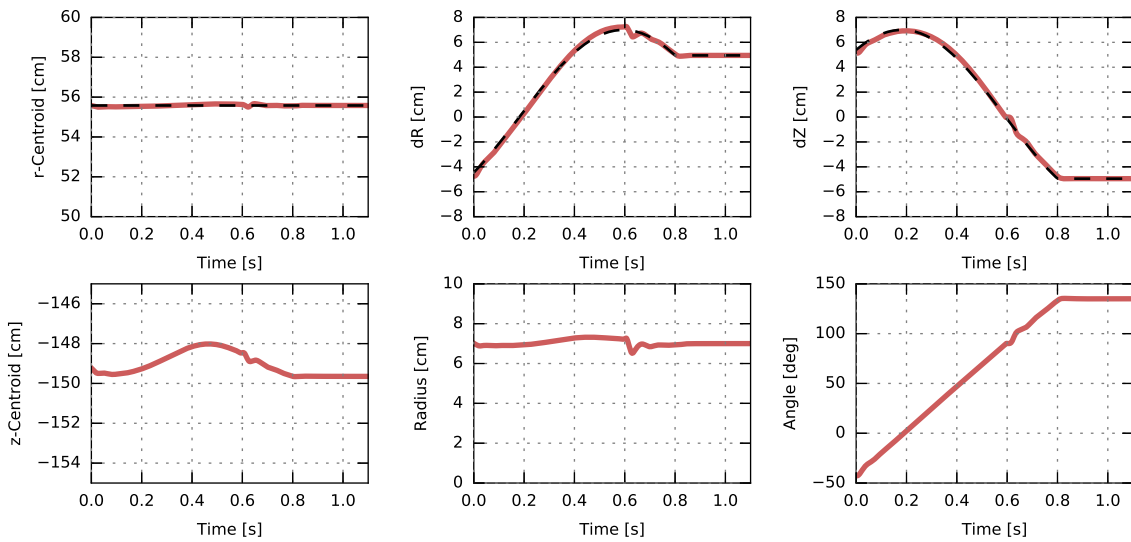


Figure 6. Time traces of snowflake parameters during a scan of the snowflake radius in SFD-plus. The crimson curves are the achieved values for the SFD configuration, while the dashed black lines in the upper row indicate the targets that were provided to the control system.

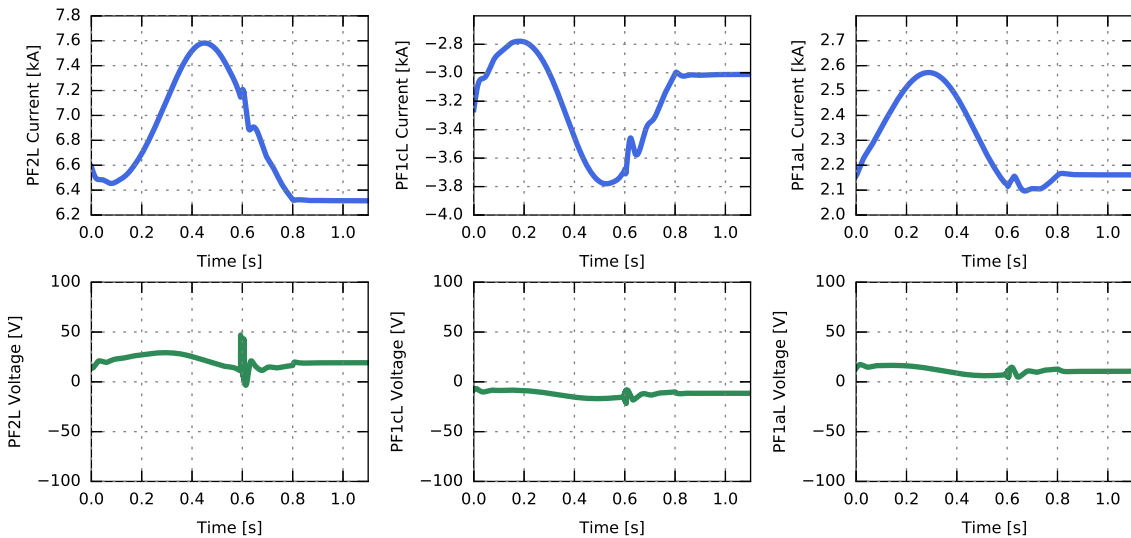


Figure 7. Poloidal field coil currents and voltages for the PF2L, PF1cL, and PF1aL divertor coils during closed-loop simulation of a scan of the snowflake angular orientation. Note that each coil has a different maximum current and available voltage. However, the maximum current and voltage for each coil are at least 13 kA and 1 kV, respectively.

with the free-boundary plasma equilibrium. The simulation was used to demonstrate the performance of the proposed SFD controller in several scenarios.

Further control development will focus on augmenting the proposed controller with additional parameters. For instance, the control scheme can be extended to include

simultaneous control of the X-point and strike point positions. Such a control scheme would be required to pursue additional advanced divertor configurations such as the X-divertor. Additional parameters of relevance to divertor operation that could be added to the control system include the poloidal flux expansion as well as the field line angle-of-incidence.

The proposed control scheme has been implemented in the NSTX-U Plasma Control System (PCS) and is ready for future plasma operations on NSTX-U using the snowflake configuration. Future experiments will study the performance of the SFD in terms of heat flux mitigation in NSTX-U.

Acknowledgments

This research was supported by the United States Department of Defense (DoD) through the National Defense Science & Engineering Graduate Fellowship (NDSEG) program as well as by the United States Department of Energy (DoE) under contract number DE-AC02-09CH11466.

Appendix

In this appendix, we derive the rigid plasma response model that is used in Section 2 to develop a linearized model of the SFD configuration response. As stated in the main text, under the rigid plasma assumption, the plasma current distribution is constrained to move rigidly in the radial and vertical directions such that the relative distribution of plasma current in the poloidal plane remains constant. The response of the plasma is therefore completely defined by the responses of r_C and z_C , the radial and vertical coordinates of the plasma current centroid. The response of the centroid position to changes in the conductor currents can be decomposed as follows,

$$\frac{\partial r_C}{\partial \mathbf{I}} = \frac{\partial F_r}{\partial \mathbf{I}} \left(\frac{\partial F_r}{\partial r_C} \right)^{-1}, \quad (1.1a)$$

$$\frac{\partial z_C}{\partial \mathbf{I}} = \frac{\partial F_z}{\partial \mathbf{I}} \left(\frac{\partial F_z}{\partial z_C} \right)^{-1}, \quad (1.1b)$$

where \mathbf{I} is a vector of (perturbed) conductor currents and F_r and F_z are the total radial and vertical forces on the plasma, respectively. Under the rigid plasma assumption, the radial and vertical forces can be expressed as follows,

$$F_r = \int (\mathbf{J} \times \mathbf{B}_{\text{vac}})_r dV + \frac{\mu_0 I_p^2}{2} \left(\ln \frac{8R}{a\sqrt{\kappa}} + \beta_p + \frac{l_i}{2} - \frac{3}{2} \right), \quad (1.2a)$$

$$F_z = \int (\mathbf{J} \times \mathbf{B}_{\text{vac}})_z dV, \quad (1.2b)$$

where \mathbf{B}_{vac} is the magnetic field generated by the conductors and the subscripts r and z denote projections of the Lorentz force in the radial and vertical directions, respectively. The second term in (1.2a) is an approximation for the outward radial force on the plasma

and is a function of the plasma current I_p , major radius R , minor radius a , elongation κ , poloidal beta β_p , and normalized inductance l_i [44].

The derivatives which are required for computing the responses of r_c and z_c can be computed directly from (1.2a) and (1.2b). For the responses of the forces with respect to changes in the conductor currents, we obtain,

$$\frac{\partial F_r}{\partial \mathbf{I}} = \int J_\phi \frac{\partial M_{pc}}{\partial r} dr dz, \quad (1.3a)$$

$$\frac{\partial F_z}{\partial \mathbf{I}} = \int J_\phi \frac{\partial M_{pc}}{\partial z} dr dz, \quad (1.3b)$$

where J_ϕ is the toroidal component of the plasma current density and M_{pc} is the vacuum mutual inductance between the plasma and the conductors. Furthermore, for the responses of the forces with respect to changes in the centroid position, we find,

$$\frac{\partial F_r}{\partial r_C} = 2\pi \int r \frac{\partial J_\phi}{\partial r_C} B_{zvac} dr dz + \frac{\mu_0 I_p^2}{2r_C}, \quad (1.4a)$$

$$\frac{\partial F_z}{\partial z_C} = -2\pi \int r \frac{\partial J_\phi}{\partial z_C} B_{rvac} dr dz, \quad (1.4b)$$

where B_{rvac} and B_{zvac} are the radial and vertical components of the vacuum magnetic field, respectively. The expressions in (1.4a) and (1.4b) can be further simplified through use of the identities $\partial_{r_C} J_\phi = -\partial_r J_\phi$ and $\partial_{z_C} J_\phi = -\partial_z J_\phi$.

The derivatives which are required for the model in Section 2 may now be computed directly from (1.1a) through (1.4b). The response of the plasma current distribution to changes in the conductor currents is computed as,

$$\frac{\partial \mathbf{J}}{\partial \mathbf{I}} = \frac{\partial J_\phi}{\partial r_C} \frac{\partial r_C}{\partial \mathbf{I}} + \frac{\partial J_\phi}{\partial z_C} \frac{\partial z_C}{\partial \mathbf{I}}, \quad (1.5)$$

while the response of the plasma flux the changes in the conductor currents is,

$$\frac{\partial \Psi_{cp}}{\partial \mathbf{I}} = M_{cp} \left(\frac{\partial J_\phi}{\partial r_C} \frac{\partial r_C}{\partial \mathbf{I}} + \frac{\partial J_\phi}{\partial z_C} \frac{\partial z_C}{\partial \mathbf{I}} \right). \quad (1.6)$$

References

- [1] MENARD, J. E., GERHARDT, S., BELL, M., et al., Nuclear Fusion **52** (2012).
- [2] GOLDSTON, R. J., MENARD, J. E., ALLAIN, J. P., et al., An Experiment to Tame the Plasma Material Interface FT/P3-12, in *Proceedings of the 22nd International Conference on Fusion Energy*, IAEA, Geneva, Switzerland, 2008.
- [3] STAMBAUGH, R. D., CHAN, V. S., GAROFALO, A. M., et al., Fusion Science and Technology **59** (2011).
- [4] MENARD, J. E., BROWN, T., EL-GUEBALY, L., et al., Nuclear Fusion **56** (2016).
- [5] ONO, M., KAYE, S. M., PENG, Y.-K., et al., Nuclear Fusion **40** (2000).
- [6] SYKES, A., AKERS, R. J., APPEL, L. C., et al., Nuclear Fusion **41** (2001).
- [7] MENARD, J. E., GERHARDT, S. P., MYERS, C. E., et al., Power exhaust scenarios & control for projected high-power NSTX-U operation, in *Proceedings of the 59th Annual Meeting of the APS Division of Plasma Physics*, Milwaukee, WI, 2017.

- [8] EICH, T., SIEGLIN, B., SCARABOSIO, A., et al., *Physical Review Letters* **107** (2011).
- [9] GRAY, T. K., MAINGI, R., SOUKHANOVSII, V. A., et al., *Journal of Nuclear Materials* **415** (2011).
- [10] EICH, T., LEONARD, A. W., PITTS, R. A., et al., *Nuclear Fusion* **53** (2013).
- [11] THORNTON, A. J., KIRK, A., and the MAST Team, *Plasma Physics and Controlled Fusion* **56** (2014).
- [12] RYUTOV, D. D., *Physics of Plasmas* **14** (2007).
- [13] KOTSCHENREUTHER, M., VALANJU, P., COVELE, B., and MAHAJAN, S., *Physics of Plasmas* **20** (2013).
- [14] VALANJU, P. M., KOTSCHENREUTHER, M., MAHAJAN, S. M., and CANIK, J., *Physics of Plasmas* **16** (2009).
- [15] LABOMBARD, B., *Bulletin of the American Physical Society* **58** (2014).
- [16] RYUTOV, D. D. and SOUKHANOVSII, V. A., *Physics of Plasmas* **22** (2015).
- [17] PIRAS, F., CODA, S., DUVAL, B. P., et al., *Nuclear Fusion* **52** (2010).
- [18] SOUKHANOVSII, V. A., BELL, R. E., DIALLO, A., et al., *Physics of Plasmas* **19** (2012).
- [19] CALABRÒ, G., XIAO, B. J., CHEN, S. L., et al., *Nuclear Fusion* **55** (2015).
- [20] SOUKHANOVSII, V. A., ALLEN, S. L., FENSTERMACHER, M. E., et al., *Nuclear Fusion*, Accepted (2018).
- [21] ASAKURA, N., SHINYA, K., TOBITA, K., et al., *Fusion Science and Technology* **63** (2013).
- [22] KOLEMEN, E., GATES, D. A., ROWLEY, C. W., et al., *Nuclear Fusion* **50** (2010).
- [23] SOUKHANOVSII, V. A., AHN, J.-W., BELL, R. E., et al., *Nuclear Fusion* **51** (2010).
- [24] HUANG, J. and MENARD, J., *Journal of Undergraduate Research* **6** (2006).
- [25] KOLEMEN, E., VAIL, P. J., MAKOWSKI, M. A., et al., *Nuclear Fusion* **58** (2018).
- [26] COUTLIS, A., BANDYOPADHYAY, I., LISTER, J. B., et al., *Nuclear Fusion* **39** (1999).
- [27] BOYER, M. D., ANDRE, R., GATES, D. A., et al., *Nuclear Fusion* **55** (2015).
- [28] BOYER, M. D., BARTON, J., SCHUSTER, E., et al., *Plasma Physics and Controlled Fusion* **55** (2013).
- [29] GOUMIRI, I. R., ROWLEY, C. W., SABBAGH, S. A., et al., *Nuclear Fusion* **56** (2016).
- [30] ARIOLA, M. and PIRONTI, A., *Magnetic Control of Tokamak Plasmas*, Springer-Verlag, 2008.
- [31] WALKER, M. L. and HUMPHREYS, D. A., *Fusion Science and Technology* **50** (2006).
- [32] RYUTOV, D. D., MAKOWSKI, M. A., and UMANSKY, M. V., *Plasma Physics and Controlled Fusion* **52** (2010).
- [33] ALBANESE, R. and VILLONE, F., *Nuclear Fusion* **38** (1998).
- [34] WELANDER, A. S., DERANIAN, R. D., HUMPHREYS, D. A., LEUER, J. A., and WALKER, M. L., *Fusion Science and Technology* **47** (2005).
- [35] FRIEDLAND, B., *Control System Design: An Introduction to State-Space Methods*, McGraw-Hill Book Company, 1 edition, 1968.
- [36] STENGEL, R. F., *Optimal Control and Estimation*, Dover Publications, 1 edition, 1994.
- [37] ÅSTRÖM, K. J. and MURRAY, R. M., *Feedback Systems: An Introduction for Scientists and Engineers*, Princeton University Press, 1 edition, 2008.
- [38] YOUNG, P. C. and WILLEMS, J. C., *International Journal of Control* **15** (1972).
- [39] FERRON, J. R., WALKER, M. L., LAO, L. L., et al., *Nuclear Fusion* **38** (1998).
- [40] GATES, D. A., FERRON, J. R., BELL, M., et al., *Nuclear Fusion* **46** (2006).
- [41] BOYER, M. D., BATTAGLIA, D. J., MUELLER, D., et al., *Nuclear Fusion* **58** (2018).
- [42] HUMPHREYS, D. A., FERRON, J. R., BAKHTIARI, M., et al., *Nuclear Fusion* **47** (2007).
- [43] LAZARUS, E. A., LISTER, J. B., and NEILSON, G. H., *Nuclear Fusion* **30** (1990).
- [44] WESSON, J., *Tokamaks*, Oxford University Press, 4 edition, 2011.